University of Trento
Department of Physics

Meep Simulations Report

Leonardo Cattarin

Laboratory of Advanced Photonics
Paolo Bettotti *Davide Bazzanella*

1 Introduction

Meep is a library for Finite-Difference Time-Domain classical electromagnetics Simulations.

The basic working principle of FDTD simulations is to discretize Maxwell's equations both in time and space, approximate the derivatives with finite differences and calculate the fields evolutions in time by iterative calculations.

Meep uses a variant of the so-called Yee's algorithm, approximating the derivatives using second-order expansions of and $\mathbf{E}$ and $\mathbf{B}$. An important aspect to keep in mind relates to the ratio of the discretization steps

$$S = \frac{\Delta t}{\Delta x} \tag{1.1}$$

called the Courant factor. It can be shown that, in order for the simulation to converge correctly, it must hold $S < n_{min}/\sqrt{\#dimensions}$. In Meep, by default $S = 0.5$

Meep uses dimensionless measurement units. This is especially useful when dealing with linear response materials: in these cases Maxwell's equations remain scale-invariant and the quantities calculated in simulations at different scales differ only by multiplicative factors.

Maxwell's equations in meep units are (with $c = 1$):

$$\frac{d\mathbf{B}}{dt} = -\nabla \times \mathbf{E} \tag{1.2}$$

$$\mathbf{B} = \mu\mathbf{H} \tag{1.3}$$

$$\frac{d\mathbf{D}}{dt} = -\nabla \times \mathbf{H} - \mathbf{J} \tag{1.4}$$

$$\mathbf{D} = \varepsilon\mathbf{E} \tag{1.5}$$

The quantities calculated during the simulations can be converted in arbitrary meaurement units just by using the appropriate factors. In the following report, some more common measurement units are used together with the "meep units" (m.u.) as a reference.

The present report contains the results of various 2D numerical simulations for three different photonic structures, composed only by dielectric materials:

- System of two coupled waveguides
- Distributed Bragg Reflector
- Microring Resonator

To simulate the presence of free space around the simulation grid, meep allows to use perfectly matched layers (PML) which are numerical boundary conditions simulating a non-physical perfectly absorbing material, provided such region is sufficiently thick.

2 Coupled Waveguides

When a dielectric waveguide is placed sufficiently near to another, the two can be coupled. This happens when the evanescent tails of some single-waveguide modes leak into the second waveguide. When one of the two waveguides is injected with some excitation, such a continuous-wave or a wave packet, the guided-mode excitations are periodically transferred into the second waveguide and back in the first waveguide again. An interesting quantity characterizing such phenomena is the **coupling length** l_c, describing the space necessary to transfer the majority of the excitation/energy density from one waveguide to the other.

The 2D geometry considered here is shown in (Figure 1), the structure parameters are presented in (Table 2) and the source parameters in (Table 3).

sx [m.u.]	sy [m.u.]	Δx [m.u.]	S	T_{sim} [m.u.]
90	7	0.05	0.5	400

Table 1: Symmetric coupled waveguides simulation parameters. From left: x size, y size, spatial resolution step, Courant factor, Total simulation time

δ_{PML} [m.u.]	W [m.u.]	d [m.u.]	δd [m.u.]	n_{bg}	n_W
1	1	[0,1.3]	0.1	3.85	4.5

Table 2: Symmetric coupled waveguides geometric parameters. From left: PML padding thickness, waveguides width, waveguides distance range, waveguide distances step for the simulation, background refractive index, waveguide refractive index

x_{src} [m.u.]	$f_{src}[m.u.]$	$t_{src}[m.u.]$
-sx/2 + δ_{PML} + 0.3	0.15	20

Table 3: Source parameters. From left: source position, source frequency, source turn-on time

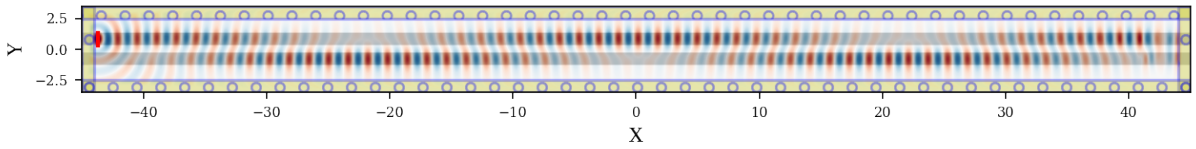

Figure 1: Geometry of the symmetric coupled waveguides

The upper waveguide (waveguide 1) is excited with a continuous-wave source, exciting only $\mathbf{E} = E_z\hat{\mathbf{z}}$. This kind of source is practically implemented as a current source $\mathbf{J}$.

The coupling length l_c is then measured with respect to the variation of various structural parameters by repeating the simulation multiple times.

l_c is here defined as the distance necessary for the E_z profile envelope at the vertical center of waveguide 1 to decrease under a certain threshold fraction of its initial initial E_z value. To evaluate such quantity, first the profile envelope is calculated from the field profile by computing its analytic signal via the **hilbert()** scipy function [1]. Using Hilbert transform, it is possible to recover an envelope $g(t)$ from a function of the shape:

$$f(t) = g(t)sin(\omega_0 t + \phi) \tag{2.1}$$

in particular, **hilbert()** computes the analytical function corresponding to $f(t)$:

$$x_a = F^{-1}[F[f(t)]2U(\omega)] = \tag{2.2}$$

$$= F^{-1}[\tilde{g}(\omega) * \frac{1}{2i}\left(\delta(\omega-\omega_0)e^{i\phi} - \delta(\omega+\omega_0)e^{-i\phi}\right)2U(\omega)] = \tag{2.3}$$

$$= F^{-1}[\frac{1}{2i}\left(\tilde{g}(\omega-\omega_0)e^{i\phi} - \tilde{g}(\omega+\omega_0)e^{-i\phi}\right)2U(\omega)] = \tag{2.4}$$

$$\approx e^{i\phi}\frac{1}{i}F^{-1}[(\tilde{g}(\omega-\omega_0))] = \tag{2.5}$$

$$\approx e^{i\phi}\frac{1}{i}e^{i\omega_0 t}g(t) = \tag{2.6}$$

Where in the last steps it has been assumed that $g(t)$ is sufficiently slowly varying (band limited and with frequency components $\ll \omega_0$).

Then the envelope can be recovered taking the absolute value:

$$|x_a(t)| = |g(t)| \tag{2.7}$$

Image (Figure 3) shows the unaltered field profiles at the end of the simulation, while (Figure 2) show the single profiles with the calculated envelopes. Notably, the reconstructed envelope produces unwanted behaviours when the field shape does not respect the assumptions, as near the source and the PML. A possible alternative is to use interpolation curves such as cubic splines on the local maxima of the field.

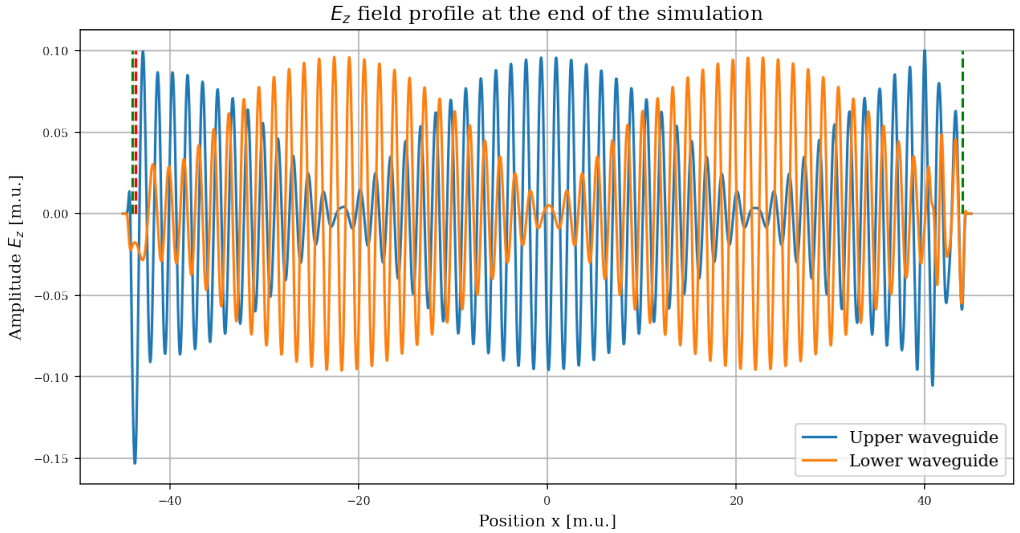

Figure 2: E_z field profiles at the center of each waveguide, taken at the end of the simulation

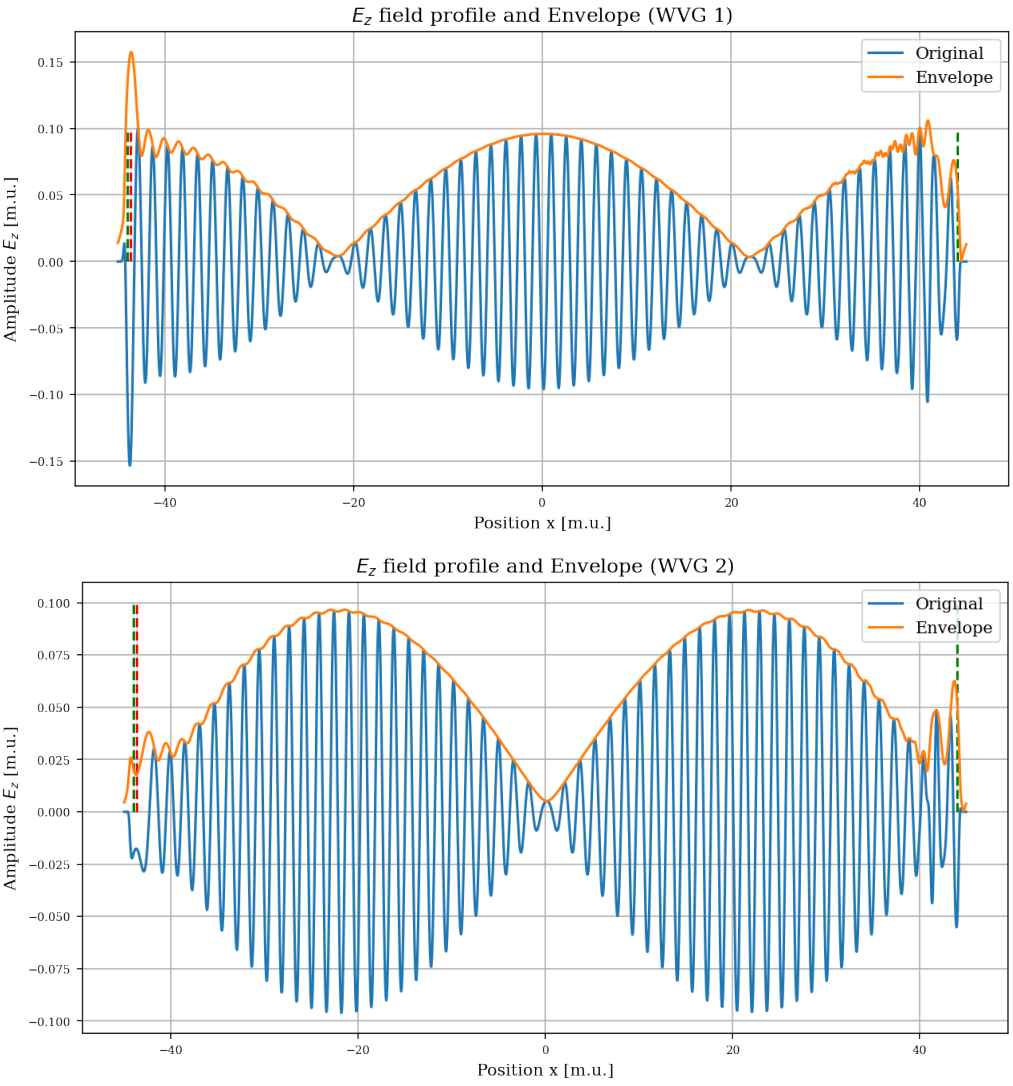

Figure 3: E_z field profiles snapshots and calculated envelopes for both the waveguides

The coupling length is then calculated by first taking all the x values inside the PML boundaries and above the x_{src} value and then filter the obtained x by considering only the values such that $E_z < \xi E_z^{init}$, with $\xi = 0.15$. Finally, the coupling length is the lowest of such x values. This is necessary to ensure that the l_c value obtained is not wrongfully calculated due to the periodic exchange of the excitation between the waveguides or due to the PML presence.

The procedure is iterated for different sets of parameters: first for different coupling distances d (Figure 4) in the range [0,1.2] [m.um], then for different waveguides widths and refractive indices (Figure 5)

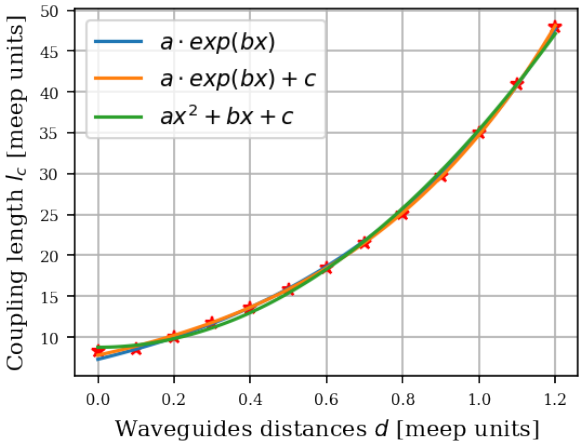

Figure 4: Coupling distances calculated for different waveguides distances

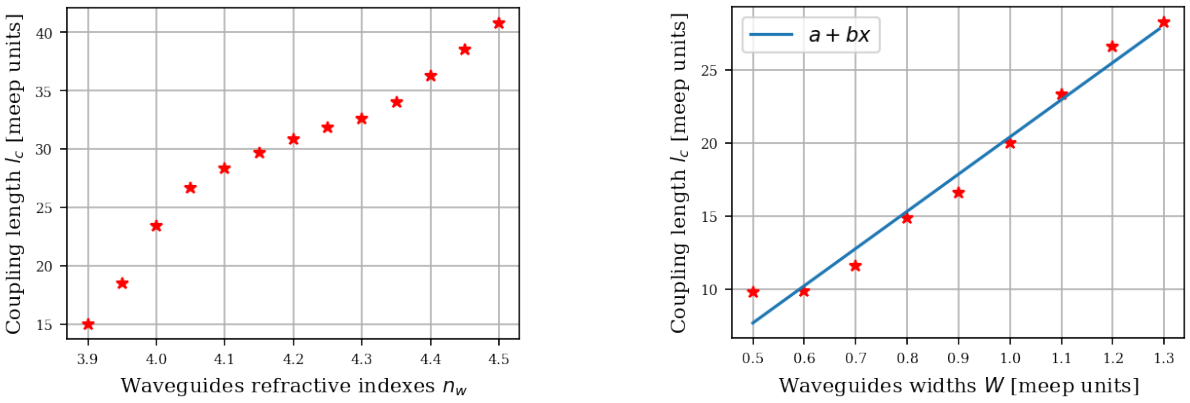

Figure 5: Coupling distances calculated for (a) different waveguides refractive index (b) different waveguides widths

3 Bragg Reflector

A Distributed Bragg Reflector (DBR) is a periodic dielectric structure composed by multiple layers of alternating dielectric materials. When an electromagnetic wavepacket or wave impinges on the device, partial transmissions and reflections happen at each dielectric discontinuity interface. As a consequence, depending on the interference effects of the

partially transmitted and reflected waves, the DBR can be used to offer highly tunable reflectivities in specific frequency regions. From an equivalent point of view, Maxwell's equation for linear dielectric systems can be recast as eigenvalue problems [2], which find analogies in quantum-mechanical problems due to the formal similarities with the stationary Schroedinger's equation. Periodic photonics devices such as the BDR are then analogous to solid state problems where an electron can be seen in an effective periodic potential. This allows to use Bloch's theorem. It further emerges that, under certain geometry parameters, some spectral frequency regions admit no modes: this phenomena is called **photonic bandgaps**. Photonic bandgaps produce spectral regions with very high reflectivity.

Here the photonic bandgaps of a 1D Bragg reflector (in 2D geometry) are studied under the variation of the refractive index contrast $\Delta n = n_1 - n_2$. The geometry considered is shown in (Figure 6) and the paramters presented in (Table 4), (Table 5), (Table 6)

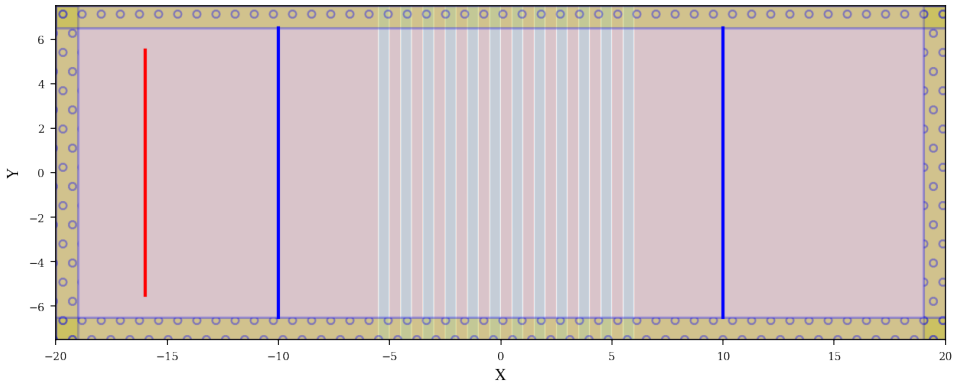

Figure 6: DBR geometry

sx [m.u.]	sy [m.u.]	Δx [m.u.]	S	ξ
40	15	0.05	0.5	5×10^{-3}

Table 4: DBR simulation parameters. From left: x size, y size, spatial resolution step, Courant factor, Simulation stop field threshold

δ_{PML} [m.u.]	δ_1 [m.u.]	δ_2 [m.u.]	n_{bg}	n_1	n_2	Δn	N_{layers}
1	0.5	0.5	1.45	n_{bg}	$n_1 + \Delta n$	[0.1,1.95]	12

Table 5: DBR geometric parameters. From left: PML padding thickness, layer 1 thickness, layer 2 thickness, background refractive index, layer 1 refractive index, layer 2 refractive index, refractive index contrast, number of compound $n_1 + n_2$ layers

The frequency response of the system is measured by exciting with a source with time-shape of a Gaussian (Equation 3.2) and measuring the incident and transmitted fluxes through monitors.

x_{src} [m.u.]	f_0 [m.u.]	Δf
$x_{low}^{bragg} - 10$	0.22	0.56

Table 6: Source parameters. From left: source position, source central frequency, source frequency width

x_{mon}^1 [m.u.]	x_{mon}^2 [m.u.]	f_0 [m.u.]	Δf_{mon}
$x_{low}^{bragg} - 4$	$x_{up}^{bragg} + 4$	0.22	0.28

Table 7: Monitor parameters. From left: position monitor 1, position monitor 2, source central frequency, source frequency width

$$s(t) \propto \exp\left[i\omega t - (t-t_0)^2/2w^2\right] \tag{3.1}$$

$$\tilde{s}(\omega) \propto \frac{1}{\Delta f} e^{i\omega t_0 - (\omega-\omega_0)^2/2\Delta f^2} \tag{3.2}$$

where $\Delta f = 1/w$ is the frequency half width. As a remark, since the pulse duration is roughly the inverse of the frequency width, using more spectrally narrow sources usually requires longer simulation times.

A monitor is a surface (1D in 2D geometries) where various fields informations can be acquired. In this case the monitors accumulate, for each monitor point $\mathbf{x}$, the discrete Fourier-transforms of the field fluxes:

$$\mathbf{f}_\omega(\mathbf{x}) = \frac{1}{\sqrt{2\pi}} \sum_n e^{i\omega n\Delta t} \mathbf{f}(\mathbf{x}, n\Delta t)\Delta t \tag{3.3}$$

where it can be $\mathbf{f} = \{\mathbf{E}, \mathbf{H}\}$.

Then, the flux power spectra is calculated by integrating over all the monitor:

$$P(\omega) = \mathrm{Re}\,\hat{\mathbf{n}} \cdot \sum_{\mathbf{x}} \mathbf{E}_\omega(\mathbf{x})^* \times \mathbf{H}_\omega(\mathbf{x}) \tag{3.4}$$

Since the monitors cannot distinguish between incidtent, transmitted and reflected waves, to correctly calculate the reflection spectra a normalization simulation is used. The transmitted and reflected spectra are calculated for a geometry where the Bragg mirror is absent, and then the "free space" $\mathbf{E}_\omega(\mathbf{x})$ and $\mathbf{H}_\omega(\mathbf{x})$ are subtracted to the monitor placed before the DBR, removing the flux components relative to the incident wave and obtaining only the reflected components. The simulation is stopped only after the source stops emitting and the field amplitude E_z at a "check" point in space decreases under a relative threshold ξ.

Image (Figure 7) shows the various measured spectra, while (Figure 8) shows the calculated Transmittance, Reflectance and Losses. The bandgap properties of interest are the central value $\omega_m = (\omega_{low} + \omega_{up})/2$ and the width $\Delta\omega = \omega_{up} - \omega_{low}$. They are calculated by first computing the first differences of the Reflectance spectra, then by identifying the two highest peaks in such graph (Figure 9), which are identified as the lower and upper boundary of the bandgap.

This procedure is expected to provide accurate results because the bandgap boundaries are assumed to be more sharp than the other spectral features, and therefore to have higher values of the first difference.

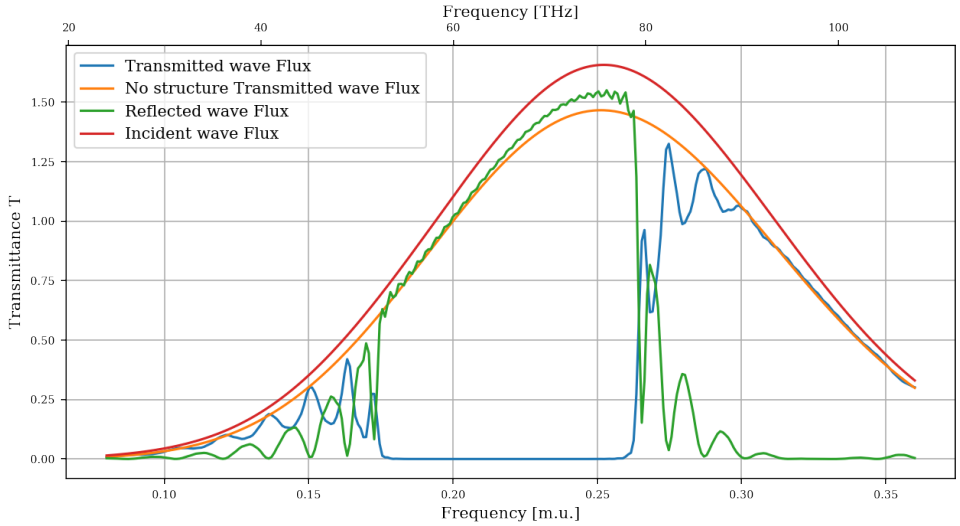

Figure 7: Measured spectra, $\Delta n = 1.6$

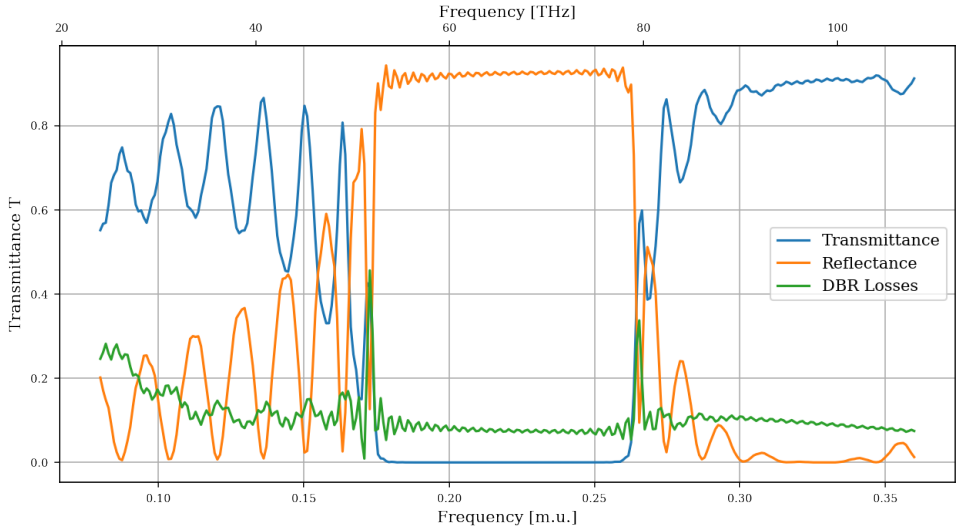

Figure 8: DBR Transmittance, Reflactance and Losses, $\Delta n = 1.6$

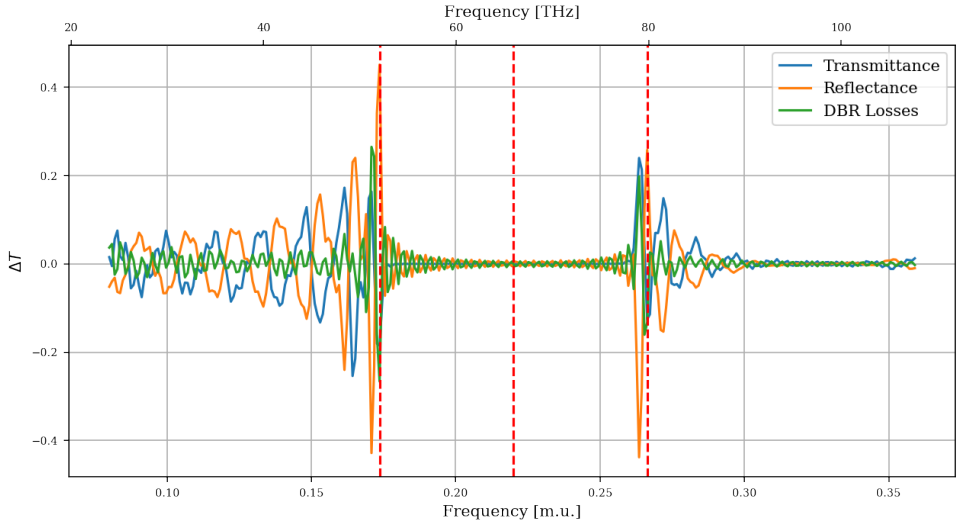

Figure 9: First difference of Transmittance, Reflactance and Losses, $\Delta n = 1.6$

The bandgap width $\Delta\omega$ and central frequency ω_M are calculated for values of refractive index contrast between the layers Δn ranging in [0.1,1.95], as shown in (Figure 11) and (Figure 10)

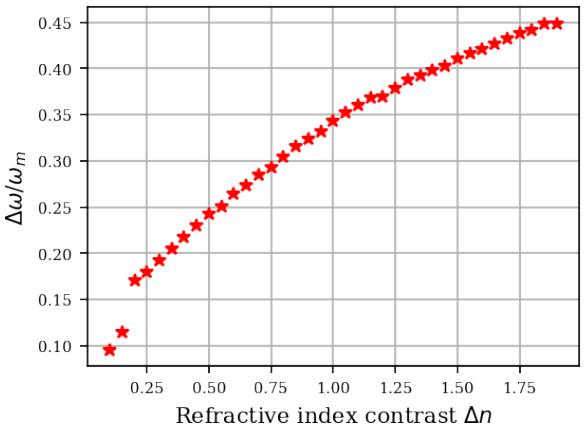

Figure 10: Normalized bandgap versus refractive index contrast of the layers

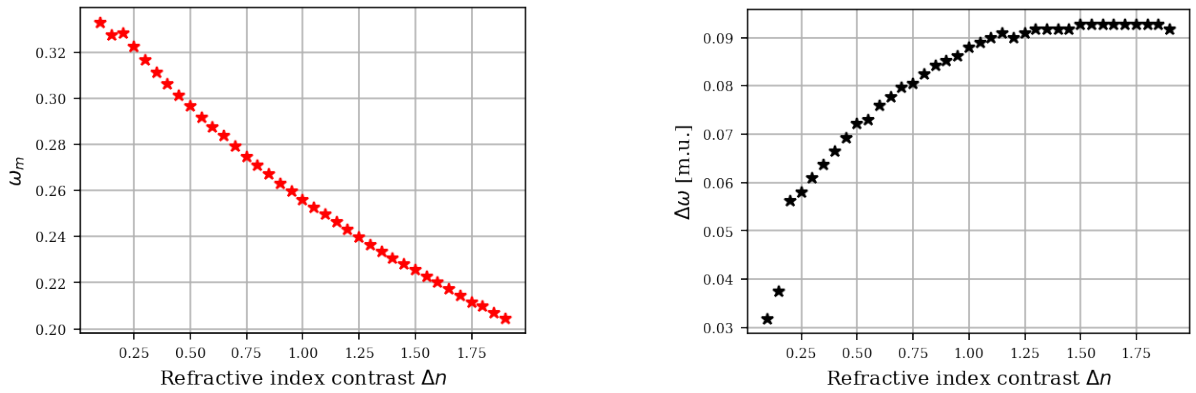

Figure 11: (a) Bandgap width versus refractive index contrast (b) Central bandgap frequency versus refractive index contrast

4 Microring Resonator

A ring resonator is a device composed by a circular crown (or ring) of different refractive index than the surrounding, often coupled with dielectric waveguides. When an excitation in the waveguide and it reaches the coupling region with the ring, it is partially transmitted to the next waveguide section and to the ring. Inside the resonator, the excitation travels in multiple round-trips and is partially lost in losses and partially re-injected in the waveguide. Due to the combined effect of interferences and losses, this device behaves as a filter a the frequencies corresponding to resonances. The behaviour of the Transmittance T and phase $\Delta\Phi$ near resonance ν_{res} are quite important in characterizing the device behaviour. Here these quantities are studied for different waveguide-ring gap distances d.

The geometry used here is shown in Figure 12 and the parameters in Table 9, Table 8, Table 11, Table 9 and Table 12.

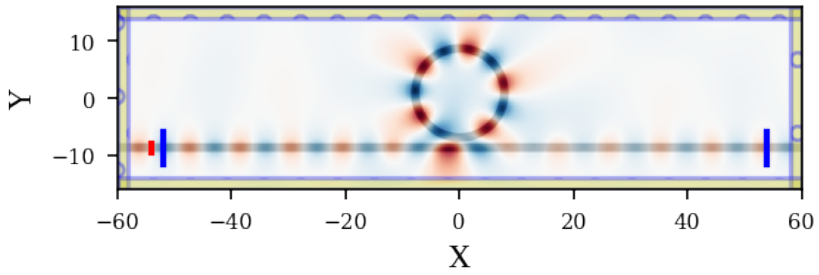

Figure 12: Ring resonator Geometry

sx [m.u.]	sy [m.u.]	Δx [m.u.]	S	ξ
120	32	0.05	0.5	10^{-3}

Table 8: Ring resonator simulation parameters. From left: x size, y size, spatial resolution step, Courant factor, Simulation stop field threshold

δ_{PML} [m.u.]	W [m.u.]	r [m.u.]	d [m.u.]
2	1.6	7	[0.1,1.15]

Table 9: Ring resonator geometric parameters. From left: PML thickness, Waveguide width, ring internal radius, ring-waveguide gap

x_{src} [m.u.]	f_0 [m.u.]	Δf_{src}
$x_{low}^{PML} + 1$	0.048	0.015

Table 10: Source parameters. From left: source position, source central frequency, frequency width

x_{mon}^1 [m.u.]	x_{mon}^2 [m.u.]	$f_0[m.u.]$	Δf_{mon}
$x_{src} + 4$	$x_{up}^{PML} - 4$	0.048	0.005

Table 11: Monitor parameters. From left: Monitor 1 position, Monitor 2 Position, central frquency, Frequency width

First, the system Transmittance is studied by using a gaussian pulse with a spectral width wide enough to capture multiple resonances, as shown in Figure 13. The resonances can also be identified using the tool Harminv, which implements the method called Filter diagonalization for the harmonic inversion problem. Essentially it performs a fit of the kind:

$$f(t) = \sum_n a_n e^{i\omega_n t} \tag{4.1}$$

where both a_n and ω_n can be complex, making each term composed potentially by an oscillating and exponentially decaying factor. Such method can be used to extract the strongest frequency components from signals taken in a point of the structure, after exciting it.

After identifying a spectrum range narrow enough to contain only one resonance, a "narrow" pulse (longer time duration) can then be used to study it, as shown in Figure 14.

In (Figure 15), the resonance shape is plotted for different values of the waveguide-ring gap d, and the transmittance at resonance for the same parameter values. As it can be noted, not only the resonance attenuation, but also the central resonance frequency changes for different d values.

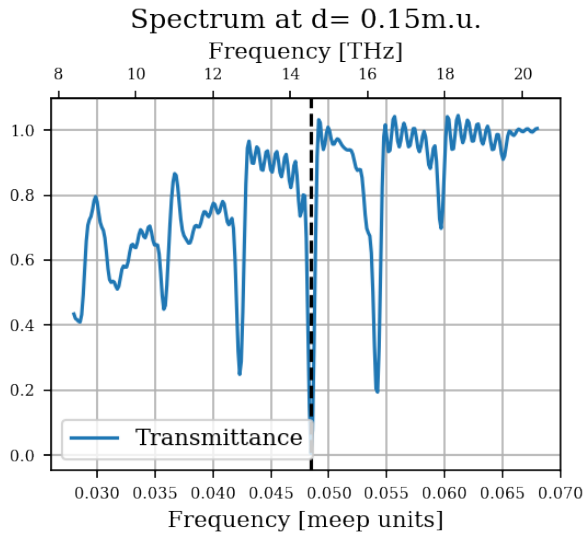

Figure 13: Ring resonator "broad" transmittance spectrum, $d = 0.15$, $\Delta f = 0.04$

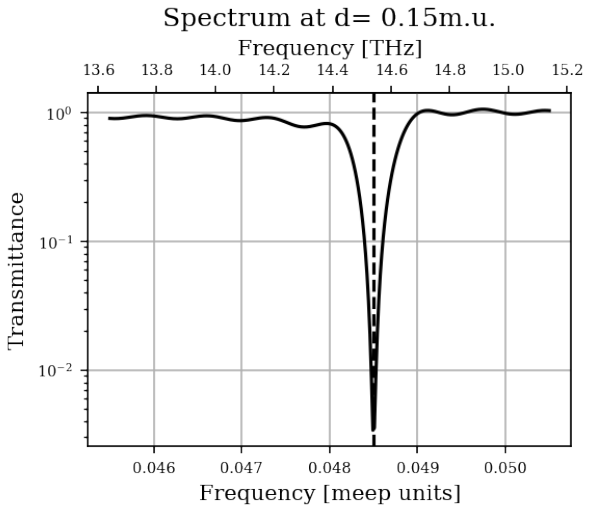

Figure 14: Ring resonator "focused" transmittance spectrum, $d = 0.15$, $\Delta f = 0.005$

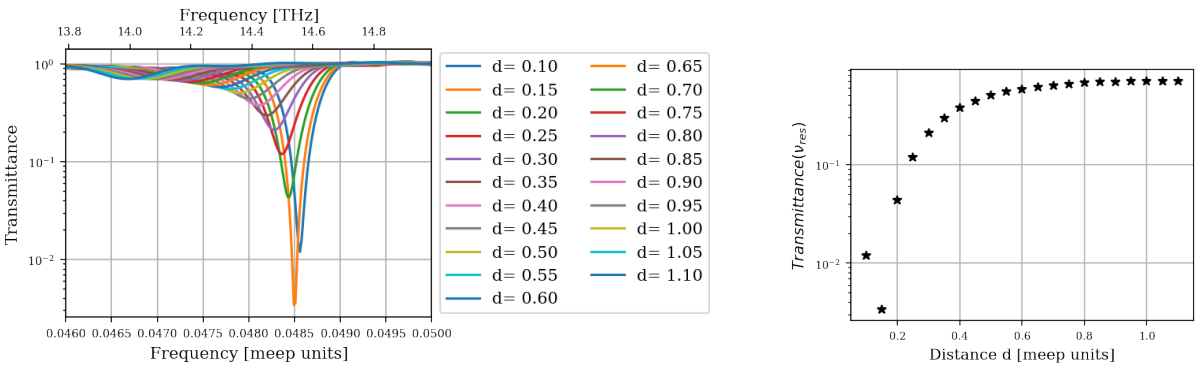

Figure 15: (a) Transmittance spectrum at different gaps d, (b) Resonance Transmittivities at different gaps d

Another interesting quantity is the phase difference $\Delta\Phi$ between an input wave and the corresponding output. To study such quantity, a different kind simulation is performed: first a continuous-wave source excites the system at the resonant frequencies ν_{res} obtained from the previous transmittance analysis. Such excitation lasts a time long enought to discard initial transient source turn-on effects.

The E_z field profile at the vertical waveguide center is then divided in regions: an initial region is used to perform a fit yielding the sine parameters for the input wave, and a final region for the output wave. Such regions are selected narrow enough and distant from the source, the coupling region and the PML layers to ensure the field profile is not distorted.

x_{low}^{init}	x_{up}^{init}	x_{low}^{fin}	x_{up}^{fin}
$x_{src} + 0.4$	-(r+W)	r+W	$x_{up}^{PML} - 0.4$

Table 12: Fit intervals for $\Delta\Phi$ calculation. The intervals are kept distant from both the coupling region, the source and the PML boundaries

The fit is performed as following: the maxima of the wave are identified, and their x_m positions are fit to arbitrary integer m values, since it holds:

$$1 = \sin(k \cdot x_m + \Phi) \Rightarrow k \cdot x_m + \Phi = 2\pi m + \pi/2 \tag{4.2}$$

$$x_m = (2\pi m + \pi/2 - \Phi)/k = \lambda m - c \tag{4.3}$$

Some examples for such fits are shown in Figure 17.

Performing such fit allows to obtain, other than the wavelength, the phases for the initial and final waves. Such phases are referred to an arbitrary reference, but this poses no problem since we are only interest in the relative phase difference $\Delta\Phi = \Phi_2 - \Phi_1$.

Plots of the original field profiles along with the fit sines are presented in Figure 18 and Figure 19. The plot of the calculated phases for the various gaps values d is finally shown in Figure 20, and can be seen to start around $\pi/2$ at small distances and decrease to 0 (as is expected for an uncoupled system). This behaviour can be interpreted, by also looking to the resonance attenuation graph, as the transition from a strong critical coupling regime to the weaker undercoupling regime.

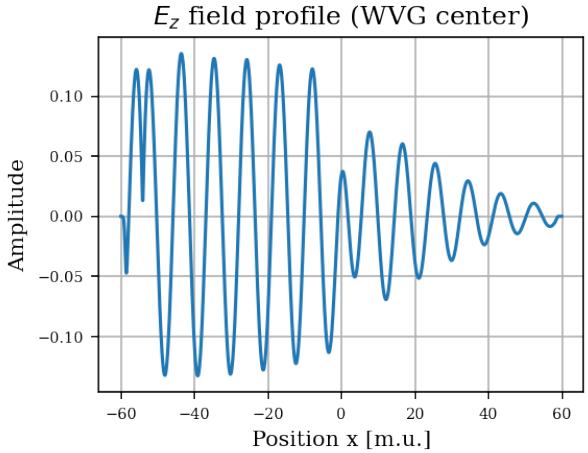

Figure 16: Complete E_z Field profile at $d = 0.15$

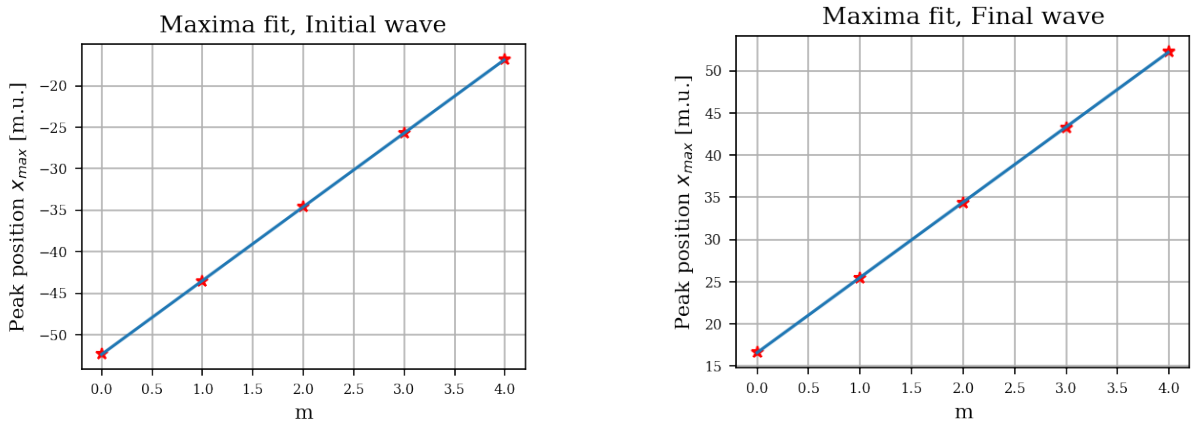

Figure 17: Fit of Peak positions vs arbitrary integers m at (a) The initial waveguide segment (b) The final waveguide segment

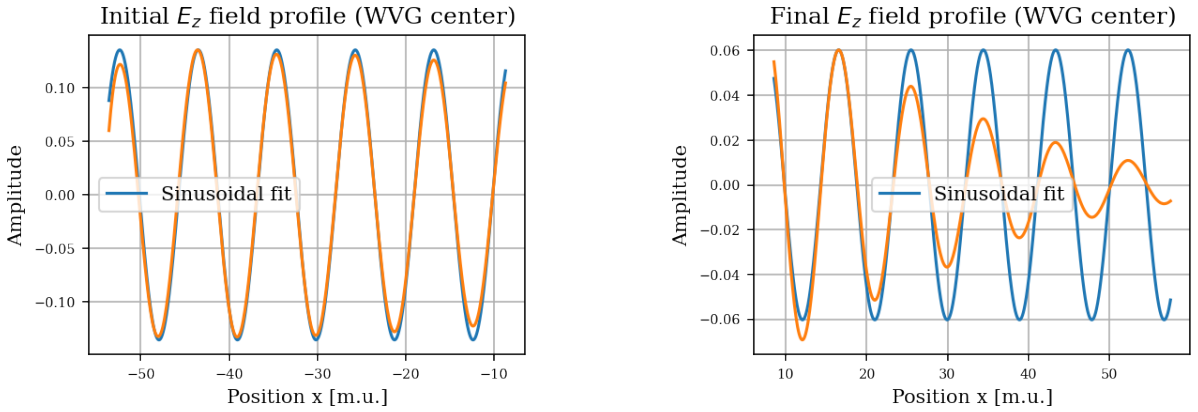

Figure 18: Fitted Sinusoids at (a) The initial waveguide segment (b) The final waveguide segment

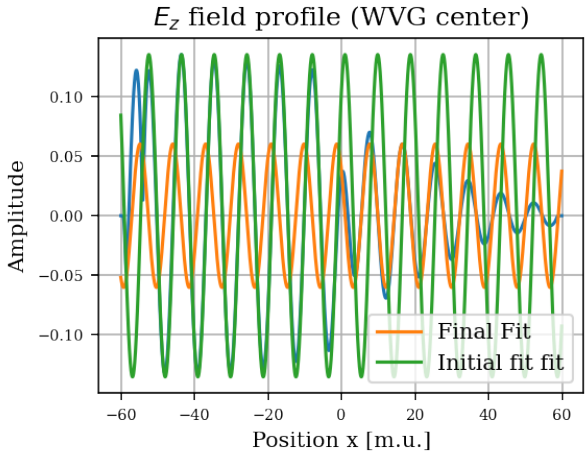

Figure 19: Fitted Sinusoids and Complete Field Profile, single comparison plot

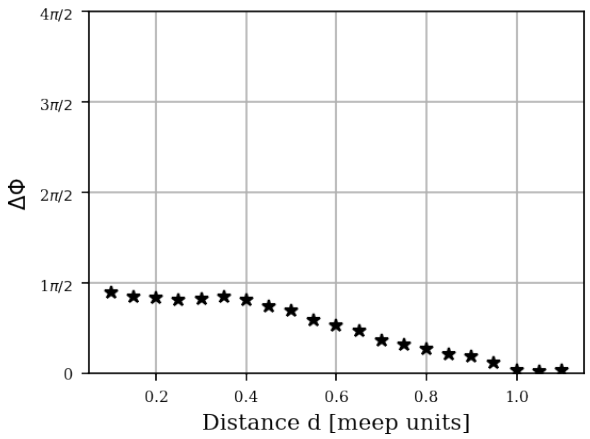

Figure 20: Phase difference $\Delta\Phi$ between input and output wave vs gap d

A Code

The code was developed in Jupyter Python Notebooks using the MEEP FDTD library, Numpy and Scipy. For each device, two notebooks were used: a Test one, used for single simulations necessary to explore the parameters and a Complete one, used to perform "definitive" simulations cycling over multiple parameters. The code is available on GitHub [3]

References

[1] *Scipy Documentation, hilbert transform*, `https://docs.scipy.org/doc/scipy/reference/generated/scipy.signal.hilbert.html`.

[2] J. John, J. Steven G., W. Joshua N. and M. Robert D., *Photonic crystals: Molding the flow of light, Second Edition*.

[3] L. Cattarin, *FDTD Meep Photonics Simulations*, `https://github.com/leonardocattarin/LabAdvPhotonicsMeep`, 2022.